



Deformation and time scales of drop dynamics in turbulent field and the effect of physical properties

Marwa S. Hamed¹ · Basim O. Hasan¹ · Hussein T. Znad²

Received: 11 March 2024 / Revised: 7 May 2024 / Accepted: 17 May 2024
© The Author(s) under exclusive licence to Associação Brasileira de Engenharia Química 2024

Abstract

The deformation scale prior to breakage and time behavior, including the maximum deformation time and the time of the total breakage cascade of two different oil drops in the turbulent field of a stirred tank, was analyzed by high-speed imaging coupled to image processing software. The effects of Reynolds number and the physical properties of drop on the deformation scale and breakage time were quantified and discussed. Different shape descriptors were used to characterize the deformation scale at the impeller vicinity, such as drop projection circularity, projection area increase, and projection perimeter extension, using image processing software. Through flow visualization, new findings concerning the effect of physical properties and Re on the critical deformation scales and breakage time were obtained. The results revealed that drop A, with a lower viscosity, experiences a lower critical deformation scale and a lower breakage time, resulting in a higher number of daughter drop at breakage. Higher viscosity drop (B) exhibited a higher critical deformation scale and higher breakage time, taking longer for breakage. About 90% of the drop deformation scale occurred at the blade's tip. The breakage time was found to be considerably influenced by physical properties of the drop. A higher impact of impeller Re on the deformation and time behavior of drop A was observed due to the lower surface stability against turbulent stresses. A highly branched morphology of deformed drop A was observed, while drop B exhibited larger elongation.

Keywords Drop deformation · Breakage time · Physical properties · Turbulence · Stirred tank

Introduction

In liquid–liquid dispersion, understanding drop dynamics in turbulent fields is crucial in various industrial applications such as liquid–liquid extraction, emulsion processing, water/oil separation in the petroleum industry, pharmaceutical industry, food industry, etc. Characterizing drop deformation behavior is of practical and scientific significance because the increased interfacial area enhances heat and mass transfer in unit operations such as mixing processes and chemical reactors. Understanding the drop deformation under different operating conditions can assist in selecting the optimum conditions for successful equipment design, reduced energy

consumption, and improving product specifications (Wang et al. 2022; Ni 2023). In multiphase flow systems, the drop breakage rate contributes effectively to mass and heat transfer phenomena owing to its direct influence on the interfacial area between the continuous and dispersed phases. The initial stage of drop breakage is deformation, which can change drop morphology and increase its surface area depending on the level of forces acting on the drop in the turbulent field. The main forces affecting the drop motion in a turbulent field are (Hinze 1955; Crowe 2005): forces exerted by turbulent eddies acting to deform and break the drop; shear force due to the difference between drop velocity and continuous phase velocity; and surface tension forces that act to hold the drop entity against the disruptive forces. The interfacial tension force tends to minimize the drop surface area, leading to a spherical shape (Andersson and Andersson 2006; Daub et al. 2013). The scale and time of deformation depend on the turbulence level (or local velocity) and on the physical properties of both the dispersed and continuous phases, such as viscosity and interfacial tension.

✉ Basim O. Hasan
basim.o.hasan@nahrainuniv.edu.iq

¹ Chemical Engineering Department, Al-Nahrain University, Baghdad, Iraq

² WA School of Mines: Minerals, Energy and Chemical Engineering, Curtin University, Perth, WA 6845, Australia

Understanding the time behavior of drops in liquid–liquid dispersion systems is vital for the successful design of these systems. A Longer time of contact between the dispersed drops and the continuous phase leads to an increase in the interaction interval, which impacts the mass and heat transfer of the process. The breakage time is considered to start when the deviation from the spherical shape reaches 10% until the moment of first breakage, at which one daughter drop separates from the mother drop (Clift et al. 2005). On this basis, the breakage is 90% of the deformation time. The breakage rate is determined from the following relation based on breakage time and breakage probability (Coualoglou and Tavlarides 1977):

$$B = \frac{1}{t_b} \frac{n}{n_T} \quad (1)$$

where B is the breakage rate, t_b is the breakage time, n_T is the number of injected drops in the turbulent field, and n is the number of breakages (normally taken as the first breakage). The fraction n/n_T is the breakage probability. Therefore, the determination of breakage time is essential for the determination of breakage rate.

An important dimensionless parameter is the Weber number (We). It describes the ratio between the fluid flow inertia and the surface tension forces and is calculated as (Hinze 1955; Clift et al. 2005):

$$We = \frac{\rho u_c^2 r_o}{\sigma} \quad (2)$$

where ρ is the density of the continuous phase, u_c the velocity of the continuous phase, r_o is the drop radius, and the σ is surface tension of the dispersed phase. Weber number is significant because it determines which force is dominant; the inertial forces of the fluid or the coherence forces that are represented by surface tension. When We is smaller than 1, the cohesive force is dominant and able to hold the drop (or bubble) entity by resisting the disruptive forces exerted by the turbulent structures. In this case, the surface tension forces try to minimize the surface area and avoid deformation. When We is larger than 1, the inertial force is dominant, and the drop can be exposed to a scale of deformation by the influences of disruptive forces that may overcome the surface tension force, breaking up the drop into smaller drops.

It has been reported in previous works (Zedel 2010; Hasan 2018a, b) that the produced daughter drops stay for a longer time in the impeller region after the first breakage undergoing further breakages due to the longer exposure to the turbulent eddies. The time interval between the first breakage and the last breakage which is termed the “breaking interval”, has been reported to be a function of flow velocity and mother drop size (Hasan and Krakau 2017). Breakage time has been reported by several studies to decrease with increasing flow velocity (Konno et al.

1983; Maass and Kraume 2012; Hasan and Krakau 2017). Other works (Solsvik and Jakobsen 2015; Zhang et al 2024) found that the breakage time has no systematic trend with flow velocity. The discrepancy in previous results regarding the breakage time is attributed to the definition of the breakage time and to complicated hydrodynamics of the turbulent field.

Literature reveals that the experimental works concerning the characterization of drop deformation in turbulent field by high-speed imaging are limited. Zhang et al. (2015) found that the addition of surfactants to the continuous phase, increases the extent of drop deformation and the way it breaks up by affecting the interfacial tension. The author noticed that the drop deformation often took a prolate shape. At relatively high concentrations of surfactant, the major to minor diameter ratio reached 1.45. Nachtigall et al. (2016) investigated the deformation of a petroleum drop crossing stationary blade as a simulation of a stirred tank. They expressed the degree of deformation by the change in the ratio between the major and minor axes and the perimeter of the deformed drop projection. At that work, a small diameter drop (1 mm) was used, therefore, the deformation ranges were limited. Despite that work provided a good understanding drop deformation in the turbulent field of stirred tank, the use of stationary blade in flowing stream conveying the oil drop is not the true case in practical application of stirred tanks. In addition, analysis of larger drop diameters is necessary to cover a wide range of particle size deformation behavior and breakage time. Wang et al. (2022) reported that the drop deformability increases with increasing viscosity ratio between dispersed and continuous phases, which affect in the transport friction coefficient. The experimental works in the literature covers a narrow range of drop deformation and operating conditions; thus, the topic still need further experimental characterization, especially under high turbulence conditions.

Several theoretical works have attempted to simulate drop deformation in turbulent flow under various operating conditions. Håkansson and Brandt (2022) performed a CFD simulation to investigate the effect of flow velocity and time on viscous drop deformation and breakage in turbulent field of emulsions. They theoretically found that the large drop experiences a high deformation scale and breaks up faster than the small one. The deformation increases with time, leading to a critical deformation at which the breakage occurs after forming single or two thin filaments, depending on the turbulence level. Håkansson et al. (2022), also reported that when the drop is deformed into two bulbs connected by a thin filament, it breaks up when the filament diameter becomes lower than the diameter of the smaller bulb. Perrard et al. (2021) theoretically found that the air bubble deformation in turbulent field of water, initially increased linearly with time and then was balanced by the effect of inertial forces and surface tension. Puncochar et al. (2022) for drop deformation in stationary water, found that the spherical drop at the release point lifts up, taking different deformed shapes such

as oblate, prolate, and spherical cup. They reported that the deformation aspect ratio (major/ minor diameter) increases with increasing Weber number.

Due to the wide range of drop breakage applications in practice, the deformation behavior still needs further investigation for complete understanding and characterization, as the literature reveals limited experimental visualization studies concerned with the deformation (Håkansson et al. 2022; Wang et al. 2022). In high-turbulence environments such as stirred tanks, the randomness of turbulent structures and flow vortices generated by the impeller cause complex local deformations and breakage behavior. This complexity is the reason behind the wide range of disagreements or discrepancies in literature findings. With the advancement of visualization techniques, high-speed imaging coupled with image processing software can play an important role in better characterizing of these phenomena. Therefore, this work employs a high-speed imaging method with image processing software to quantitatively characterize the scale of deformation and time of the breakup behavior of two different types of oils in the turbulent field of a stirred tank.

Experimental work

Material and methods

Figure 1 shows the schematic diagram of the experimental setup. The apparatus comprised a cylindrical baffled tank

made from acrylic glass. The cylindrical tank is surrounded by an external rectangular glass tank used to avoid light reflections and scattering when recording the videos by high-speed camera. Two baffles were installed inside the cylindrical tank to avoid the formation of vortices on the free surface. A digital mechanical stirrer model (BL610D) was connected with a stainless-steel shaft attached to a 4-flat blade impeller (Rushton turbine) used for providing different agitation speeds. High-speed camera (Phantom Miro-C110) was used to chase the drop motion from the injection moment until crossing the impeller region. Light emitting diodes (LED) were used for the illumination. A syringe pump was used to control the oil drop injection rate. Table 1 presents the dimensions of the components of the experimental rig. Two values of stirring speeds were used, namely, 75 and 150 rpm. The Reynolds number corresponding to each speed was calculated based on the impeller's diameter and on the physical properties of the continuous phase at room temperature (25 °C):

$$Re = \frac{\rho D_i^2 N}{\mu} \quad (3a)$$

D_i is the impeller diameter, N is the rotational speed, and μ and ρ are the viscosity and density of the continuous phase (water). The values of Re for each rotational speed were 6110 and 12230, respectively. The impeller was made of transparent acrylic material to allow tracking the drops even when they went behind the blades or between them. The impeller was located at a distance of 163 mm above

Fig. 1 1-Computer, 2-Syringe pump, 3-High speed camera, 4-Stirrer, 5-Injection tube, 6- Oil drop, 7- Acrylic rectangular tank, 8-Baffles, 9- Light source, 10- Acrylic cylindrical tank, 11- Stand

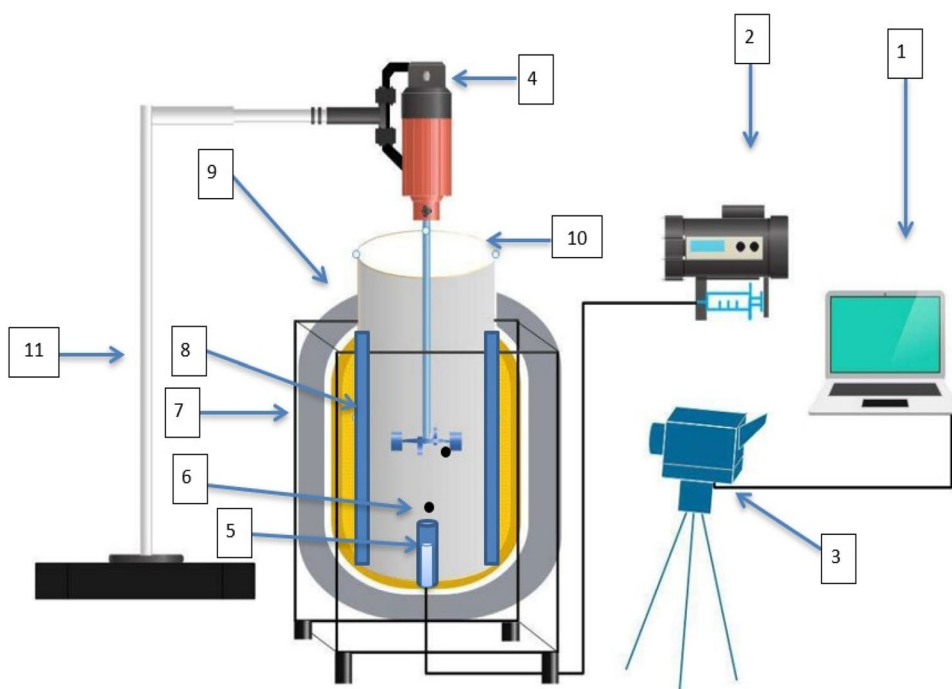


Table 1 Dimensions of stirred tank and drops injection setup

Parameter	Value
Tank diameter, (DT), mm	180
Tank height, (H), mm	400
Impeller Diameter, (Di), mm	60
Blade width, (W), mm	20
Blade length, (L), mm	20
Blade thickness, mm	2.0
Off-bottom clearance, (C), mm	163
Number of baffles, (Nj)	2.0
Width of baffle, (WBF), mm	18
Baffle thickness, mm	2.0
Impeller disc diameter, (DC), mm	50
Shaft diameter, (DS), mm	8.0
Diameter of sparger tube, mm	4.0
Diameter of framing tube, mm	10
Dimensions of external tank, mm	250×250×400

the injection tube. An external tube was used to surround the injection tube to prevent the drop from being detached earlier (Hasan and Krakau 2017). The injection tube was placed beneath the impeller in the center of the tank's bottom to ensure the mother drop goes to the impeller region.

The high-speed camera was positioned normal to the stirrer shaft, covering the area from the initial deformation at injection point until the drop has left the impeller region where no further deformation or breakages. The camera had a maximum resolution of 1280×800 pixels and a recording speed of 1200 frames per second (fps) at that resolution. Frame rate of 1000 fps was found to be sufficient to capture the deformation scale, time ranges, and number of breakages and their locations relative to the impeller. The exposure time was set on 110 μs. LED of 1000 watts was used for the illumination, placed in a location opposite the camera (backlight illumination). The mother drop diameter was consistent between all experiments and was measured to be 6.5 ± 0.4 mm. "Image J software, V 1.8.0" was used for image processing and analysis of the drop deformed shapes. The reference object was the diameter of impeller shaft for the drops close to the impeller and was the injection tube diameter for the injected mother drops. The drop injection rate was 1 drop per minute. At least 300 injection tests were considered for each experimental condition. This was found

Table 2 Experimentally measured physical properties of oils at room temperature (25 °C)

Oil	Type	Dynamic viscosity, kg/m.s	Density, kg/m ³	Surface tension, mN/m	Interfacial tension, mN/m
A	Crude oil (Basra oilfield)	18.1 (Apparent viscosity)	890.0	28.5	27.4
B	Lub. Oil (Al-Dura Refinery)	123.3	860.1	32.0	30.2

Table 3 Values of Weber number for both oils

rpm	Re	We, drop A	We, drop B
75	6110	8.8	7.5
150	12230	35	31

to be sufficient to give statistically significant results. Water is the continuous phase with a density of 998 kg/m³ and a viscosity of 0.001 Pa·s at a laboratory temperature of 25 °C ± 2 °C.

Two oils of different physical properties were used: crude oil of Basara oilfield in Iraq (oil A) and lubricating oil of Al-Dura Refinery (oil B). The physical properties of the two oils are measured experimentally and listed in Table 2. The density of oils was measured at room temperature by two methods to ensure the repeatability of the result. The first method was Anton Paar Portable Density Meter (DMA™ 35) and the second method was by using pycnometer. The viscosity was also measured by two methods; the first was by NDJ S5 Digital Viscometer with different spindles depending on the oil viscosity. The second method was by using a viscometer tube with the Tamson (PMT) manufactures of very stable temperature bath that allows the user to determine viscosity in a very precise way. The surface tension was measured by a K6 tensiometer, using the du Nouy platinum-ring method.

Based on the physical properties listed in Table 2, the values of *We* are calculated using Eq. (2) for an average mother drop diameter of 6.5 mm, and presented in Table 3. Since the values of *We* are greater than 1, the inertial forces are dominant for both oil drops, and the drops are prone to deformation and breakage.

Shape descriptors for deformed drops

The increase in deformation scale of the drop was captured by high-speed camera from the injection point until it arrived at the impeller region. The time of deformation was also recorded by high-speed camera time recording with precision of 0.01 microsecond, i.e. 10⁻⁸ s. Highly deformed shapes were observed, requiring careful analysis with suitable shape descriptors to express the degree of deformation under different operating conditions. Because the results showed a highly deformed shape, the aspect ratio (major axis/ minor axis) is not suitable for representing the

deformation scale in this work. Image processing was used to analyze the deformed shapes and obtain the values of these shape descriptors for both oil drops for the entire range of Re. The shape descriptors were based on the projection area of the drop in a two-dimensional image recorded by the camera. The following shape descriptors are considered:

- (1) Circularity, calculated as follows

$$\theta = \frac{4\pi A}{p^2} \quad (3b)$$

where A is the projection area, p is the projection perimeter. The circularity for the circle is 1. Both projection area and projection perimeter of the deformed shape is estimated by "Image J software" from the morphology of the shape.

- (2) Projection area of the deformed shape relative to the area before deformation. The area of original circular shape and of the deformed shape is estimated by "image J software". The projection area ratio (PAR) = area of the deformed shape/area of original circular shape.
- (3) Projection perimeter of the deformed shape relative to the perimeter before deformation.

Image processing procedure

The image processing was carried out using "Image J Software, V 1.8.0" to obtain quantitative information from the raw image of the drop, for characterizing the drop deformation behavior. The aim was to determine three aspects: deformed shape morphology, drop diameter, and the shape descriptors (circularity, perimeter, and surface area). For this target, the image processing included the following steps:

- 1- The drop's raw image was opened using the Menu Bar of Image J window; File > Open.
- 2- The image processing software was set to the required parameters. The setting was accomplished by using the toolbar option: Analyze > Set Measurement; to select the required parameters, such as perimeter, area, and circularity (through the shape descriptor option).
- 3- The true dimension of the reference object was provided to the software using: Analyze > Set Scale. At this stage, the true dimension of the impeller's shaft was given in mm, which was the basis for all measurements. The pixel dimension of the reference object (the shaft) was also measured by drawing a straight line between the two edges of the shaft's image. Then, the option: Analyze > Measure, was used to obtain the length readily. This length was provided to the software to use in the next measurements.

- 4- The deformed drop image was processed using: Image > Type > 8 bit. Then: Image > Adjust > Threshold. The processing was continued by converting the image into (black and white). Then, the option: Analyze Particle > Display Results, was used. At this stage, all the required measurements were displayed by the software in a result window with a colored image of the deformed drop.
- 5- Drop diameter is measured by using a straight-line tool on the toolbar, and then: Analyze > measure, to display the results readily. The number of daughter drops was counted by mere sight, as it was easy to do.
- 6- On some occasions, especially when the contrast between the drop and the background was not high, some software tools were used, such as: Process > Enhance Contrast, Process > Sharpen, Process > Subtract Background, and Process > Noise > Despeckle.
- 7- For the case of an elongated bended drop or a drop taking a tortious shape, the length of the elongated drop was measured using the "segmented line tool" presented on the toolbar of ImagJ.

The image processing of the crude oil drop was easier than the lubrication oil drop because the crude oil drop was black, which gives a high contrast with the white background. The steps mentioned earlier were used for the drop before and after deformation to calculate the change in the shape descriptors and observe the morphology variation.

Uncertainty of experimental results

The uncertainty in the experimentally measured quantities comes from two sources: the first is the accuracy of measurements, and the second is the unavoidable random error of experimental condition control. It is necessary to specify the propagated errors from these two sources. The results' uncertainty is expressed using average deviation calculated as (Herzog 2019):

$$\text{Av. Deviation} = \frac{1}{n} \sum_1^n |X - X_{av}| \quad (4a)$$

where n is the observation number, X the value of observation, X_{av} mean of the observations. The percent average deviation is the average deviation expressed as a percentage of the mean:

$$\% \text{ Av. Deviation} = (\text{Av. Deviation}/X_{av}) \times 100 \quad (4b)$$

The experimental uncertainty were represented by:

- 1- Inaccuracy in the real dimensions of the deformed drop as the image is taken in two-dimensions not in three dimensions. In addition, during image processing, increasing the

contrast between the drop and the background to subtract the background image from the drop image (especially when the blade appears in the background), might cause missing of some pixels, leading to error in the dimensions of the deformed drop. This error was reduced by analyzing a sufficiently high number of drop images. Up to 100 images were analyzed to determine the average values of the shape descriptors for each Re of both oil drops. The average deviations based on this number of observations were calculated using Eq. (4b) and expressed as error bars on the results' figures. It was within 10–18%. This percentage is acceptable for the current system because of the complicated hydrodynamics and high random motion of turbulent structures.

- 2- Inaccuracy in mother drop size measurements when it became far from the reference object, which was the impeller shaft. In this case, the blade dimension was also used as a reference object when it was closer to the drop location. At the injection point, the injection tube diameter was used as a reference object. By comparing a measured size for a certain drop relative to these three reference objects, it was found that the average deviation percent calculated using Eq. (4b) was 0.5%.
- 3- Error related to the accuracy of stirrer speed. The speeds were calibrated via the high-speed camera. The average deviation in the speed measurement (according to Eq. (4b)) was about 0.48%.
- 4- Errors arise when measuring the physical properties of the oils. These errors were minimized by carrying out each test three times. The average deviation (according to Eq. (4b)) was about 1% for both oils.
- 5- Error due to the image distortion caused by light reflection caused by the acrylic wall reflection effect. It was estimated by determining the dimension of a known object using the image processing method, and found that the error percent between the real value and that taken by the camera was 0.4%.
- 6- Inaccuracy in the number of daughter drops generated, because some of these are too small below the camera detectable size. These were very few because the camera captured very small diameters as small as 0.07 mm. This small size was only seen at the highest stirring and was estimated by counting the number of drops of this size. It was found to be 1% of the total number of drops. Therefore, the percentage of smaller diameter drops that could be missed is lower than this percentage (< 1%).

- 7- Error in controlling the size of the injected mother drop, because it may be realized before it reaches the specified size due to the shearing effect of flow currents, especially at high rotation speed. This was reduced by using a framing tube (Hasan and Krakau 2017). Based on the analysis of a sufficient number of drops, it was found that the maximum size deviation was 6% for the whole range of stirring speeds for both oils.

Results and discussion

Deformation scale

Critical deformation

It has been observed by high-speed imaging that the drop experiences a different deformation scale before breakage. However, not all deformations lead to the occurrence of breakage, as the drop can restore its spherical shape after a large degree of deformation. The scale of deformation is found to depend on the impeller rotation speed (or Re) and on the physical properties. When the drop detaches from the injection tube, it takes on a spherical shape due to the effect of surface tension (Fig. 2). During its rise by buoyancy forces and when starting to approach the impeller, the deformation starts. The deformation at which the drop cannot restore its original form is the critical deformation, as has been termed previously (Andersson and Helmi 2014; Karimi and Andersson 2020; Håkansson and Brandt 2022).

The average circularity of the injected drops, estimated by image processing at the injection position, is found to be within 0.93–0.95 mm. When the drop lifted up by buoyancy forces its deformation increases slightly until it approaches the impeller. When the drop becomes very close to the blade, its deformation scale increases appreciably depending on impeller Re and drop physical properties. Figure 3 shows a typical example of how the deformation scale of crude oil drop (A) increases from the injection point until it reaches the impeller blades at Re = 12230. It can be seen that at the injection position (P_0) to about $\frac{1}{4}$ the distance between the injection position and the impeller (at P1), the mother drop is spherical with circularity of more than 0.9. At about mid-distance, the deformation begins to increase, leading to a decrease in the circularity and an increase in the projection area and projection perimeter. When the drop becomes very

Fig. 2 Projection area ratio = A_2/A_1

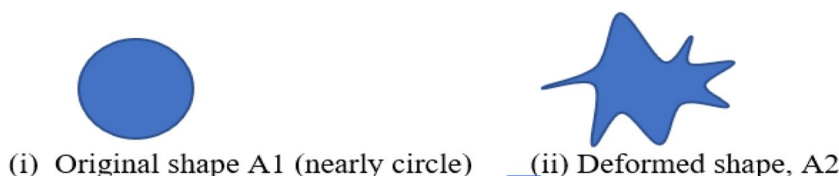
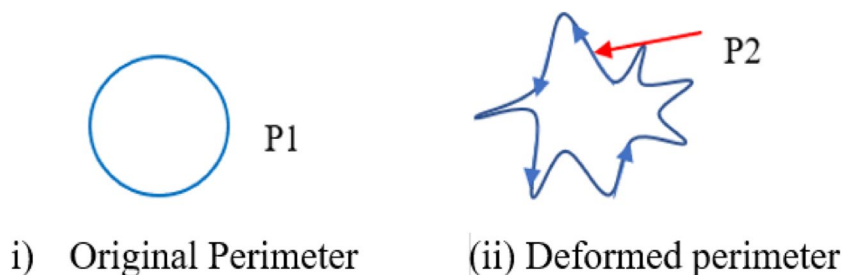


Fig. 3 Projection perimeter ratio (PPR) = $P2/P1$



close to the blade bottom, the deformation increases, further as indicated by the decreased circularity and increased projection area and perimeter. Until this stage, the decrease in circularity is not large indicating low deformation. When the drop enters between the blades, it experiences high deformation, leading to a high decrease in the circularity and a high increase in the projection area, and perimeter and its morphology becomes highly deformed. It can be seen that the circularity decreases from 0.89 (at P2 at $t=t_0$) to 0.12 at P4 where the first breakage occurs and the first daughter drop is separated from the mother drop. The time interval taken from the circularity of 0.89 to the first breakage is 260 ms. This is the breakage time according to the definition of Clift et al. (2005) which was also adopted by subsequent researchers (e.g., Konno et al. 1983; Maass and Kraume 2012; Hasan and Krakau 2017).

The visual observation via high-speed camera shows that when the deformation is high (at high impeller speed), the drop can take different complicated morphologies. Tables 4, 5 and 6 present typical examples of the morphology of different deformed shapes at the moment prior to breakage (or at critical deformation) for both oils for the values of Re investigated. The values of shape descriptors and the number of drops produced after the breakage for each morphology are also presented. Table 4 for oil A at $Re=6110$ shows that when the drop approaches the impeller, it can take various deformed shapes including elongation, thinning, necking, dumbbell shape, two bulbs connected by neck (Fig. 4).

In Table 4, the maximum deformation is expressed by the high values of deformation descriptors, such as in a few cases, the decrease in circularity reaches 0.14 with the highest increase in the projection perimeter by 3 times that of the mother drop before deformation, and in the projection area by 1.9 times.

Table 5 for oil A at $Re=12230$, shows more complicated shapes than those at $Re=6110$, such as shapes with many branches, higher stretching, higher elongation with high roundness, and higher thinning. In Table 5, the deformation can reach high values such as: circularity of 0.09, PAR of 2.8, and PPR of 4. It can be seen from Tables 4 and 5 that there are a few occasions at $Re=6110$, give deformation parameter higher than that at $Re=12230$. This is attributed to the location of the mother drop relative to the blade.




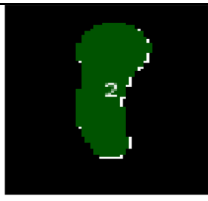





Closest drop to the blade gives higher deformation than far ones.

Table 6 presents the deformed shapes and scales of Lub. Oil (B) having higher viscosity and surface tension at $Re=12330$. The shapes are also highly deformed, exhibiting high elongation, thinning, and roundness. The individual deformations indicate a range of shape descriptor values. On some occasions, oil B exhibits higher deformation values than the maximum deformation seen for oil A such as circularity of 0.07, PAR of around 2.9, and PPR = 5.5. Despite the fact that oil B exhibits a higher critical deformation scale than oil A, the number of generated daughter drops for B is much lower than that for A.

Tables 4, 5 and 6 reveal that, in general, the number of produced drops is often increases with the critical deformation scale. However, in some cases, lower deformation produces a higher number of daughter drops than higher deformation or vice versa. At $Re=12230$, it is evident that the stretching of drop B is generally high compared to crude oil A. The maximum increase in perimeter for drop A is 4.4 (shown in Table 5) and 5.5 for oil B (shown in Table 6).

Figures 5, 6, 7, 8 and 9 show the values of different shape descriptors for different impeller Re for both oils. These values are at the moment prior to breakage when the deformation is at its maximum, i.e., critical breakage. The values represent the average of the analysis of 100 deformed drops using image processing software. Figure 5 presents the behavior of the average value of projected area circularity (PAC). It indicates that the circularity decreases with increasing Re for both oils. It can be seen that for drop A at $Re=6110$, the average PAC is 0.35, and at $Re=12230$, it is 0.228 (i.e., 35% reduction). The relevant values for drop B are 0.24 and 0.19 at the two Re respectively (21% reduction). This behavior indicates that for higher Re, the critical deformation scale is higher, and the effect of Re on drop A deformation is higher than on drop B. Figure 6 presents the average area ratio of the projection of the deformed shape at critical deformation to the original projection area of spherical drop before the deformation (when the circularity is greater than 90%). It can be seen that the PAR increases with increasing Re for both oils. Figure 6 indicates that for oil A at $Re=6110$, the average projection area of deformed shape relative

Table 4 Deformed shapes and shape descriptors by image processing, crude oil (A), $Re=6110$

No.	Deformed shape	PAR	PPR	Deformed circularity	No of daughter drop
1		1.2	1.9	0.42	2
2		1.9	3.0	0.14	4
3		1.5	2.5	0.20	5
4		1.1	1.8	0.50	2
5		1.6	2.4	0.62	2
6		1.3	2.1	0.50	3
7		1.8	2.9	0.21	5
8		1.1	1.7	0.39	4
9		1.5	2.2	0.32	5

to the original area of circular shape (the projection area ratio, PAR) is 1.52, i.e. the projection area increases by 52% due to the deformation to reach the first breakage

moment. Similarly, for $Re=12230$ the PAR is 1.88, i.e., the average increase in the area of drop A is 88% to reach the first breakage moment. The relevant values of drop B

Table 5 Deformed shapes and shape descriptors by image processing, crude oil (A), $Re = 12230$.













No.	Deformed shape	PAR	PPR	Deformed circularity	No of daughter drop
1		2.1	3.2	0.24	7
2		1.6	2.4	0.19	44
3		1.7	2.5	0.16	57
5		2.8	4.0	0.11	40
6		1.9	2.6	0.10	35
7		2.2	3.3	0.09	27
8		2.5	3.6	0.12	43
9		1.9	3.1	0.19	35
10		1.7	2.4	0.11	26
11		1.9	2.8	0.13	49
12		2.3	3.3	0.14	54
13		2.5	3.7	0.21	65

Table 6 Deformed shapes and shape descriptors by image processing, Lub. oil (B), $Re = 12230$.





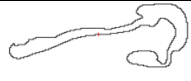









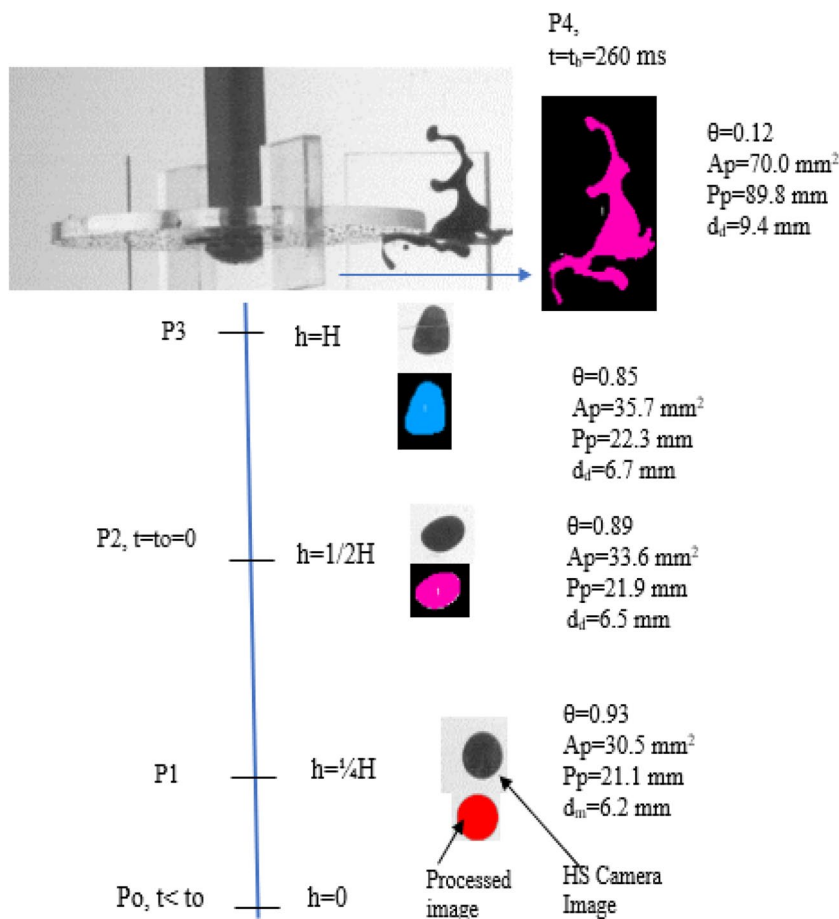
No.	Deformed shape	PAR	PPR	Deformed circularity	No of daughter drop
1		2.2	4.1	0.15	12
2		1.5	2.6	0.16	4
3		1.6	2.6	0.38	4
4		1.25	2	0.29	33
5		1.6	2.7	0.31	4
6		2.2	2.9	0.11	18
7		2.0	3.7	0.2	7
8		1.9	3.6	0.29	6
9		2.2	4.3	0.12	16
10		2.9	5.5	0.07	20
11		2.1	4.0	0.12	5
12		2.0	3.6	0.10	19
13		2.1	3.6	0.17	22
14		2.8	4.6	0.17	3
15		2.4	4.0	0.09	19

Fig. 4 Typical example of drop deformation stage when approaching the impeller



are 80% and 200%. Hence, the change in projection area indicates that higher deformation for drop B is required to reach the breakage than that of drop A. In addition, when Re increases from 6110 to 12230, the increase in PAR for drop A is 24% and for drop B, is 19% for B.

Figure 7 shows the behavior of the projection perimeter of a deformed drop prior to the moment of breakage (i.e., at critical deformation) to that of the original circular drop (i.e., projection perimeter ratio, PPR) for different Re of both oils. It indicates that PPR increases with Re for both oils.

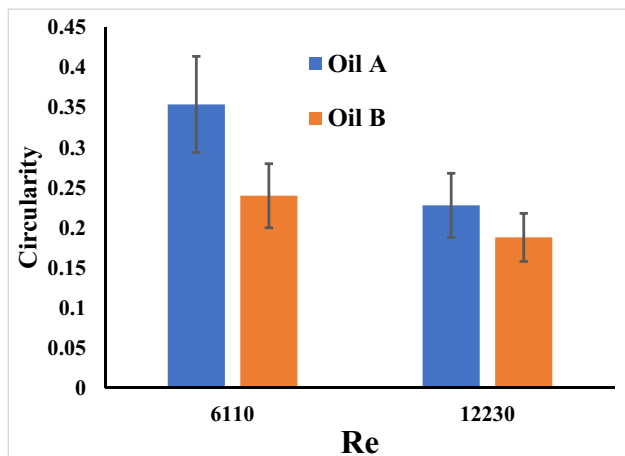


Fig. 5 Circularity vs. Re of the deformed shapes prior to breakage (error bars = av. deviation)

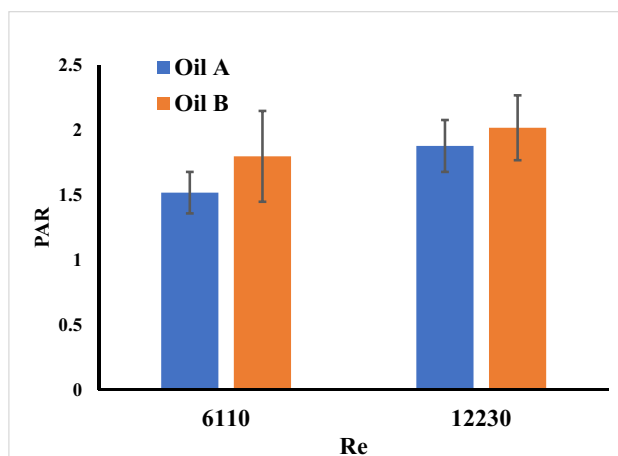


Fig. 6 Projection Area Ratio vs Re prior to breakage (error bars = av. deviation)

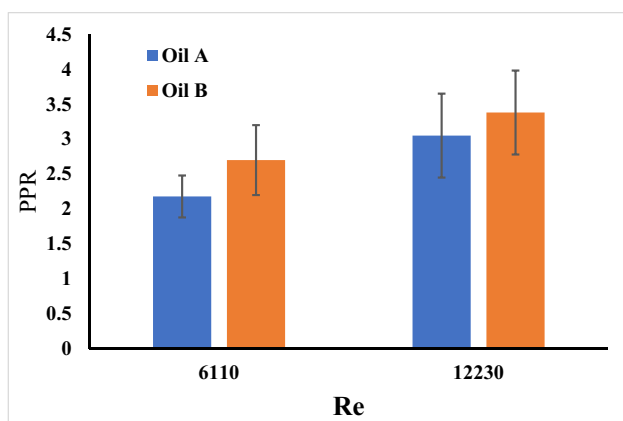


Fig. 7 Projection perimeter ratio prior to breakage (error bars = av. deviation)

It can be seen that at $Re=6110$, the PPR of A is 2.18, i.e., the perimeter of the deformed drop increases by 218% to reach the moment of breakage. At $Re=12230$, it is 3.05, i.e., the PPR of drop A increases by 305% to break up. The relevant increase for oil B is 252% and 338% for the two Re , respectively. Figure 7 indicates that when Re increase from 6110 to 12230, the increase in PPR for is 40% for A and 34% for B, indicating that the effect of Re on is higher on A deformation than on B.

Overall, the three shape descriptors in Figs. 5, 6 and 7 agree that, to reach the breakage stage, a higher deformation scale is required for drop B (of higher viscosity and surface tension) than that of drop A. Additionally, increasing flow velocity or Re , causes higher deformation for the lower viscosity oil (A). Figure 8 presents the average number of generated daughter drops versus Re for the two oil mother drops. It can be seen that the number of daughter drops increases clearly with Re and is much higher for A. This indicates that when the drop is easily deformed, it produces a higher number of fragments.

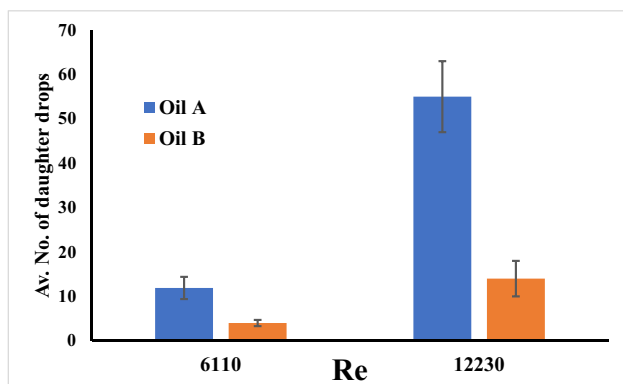
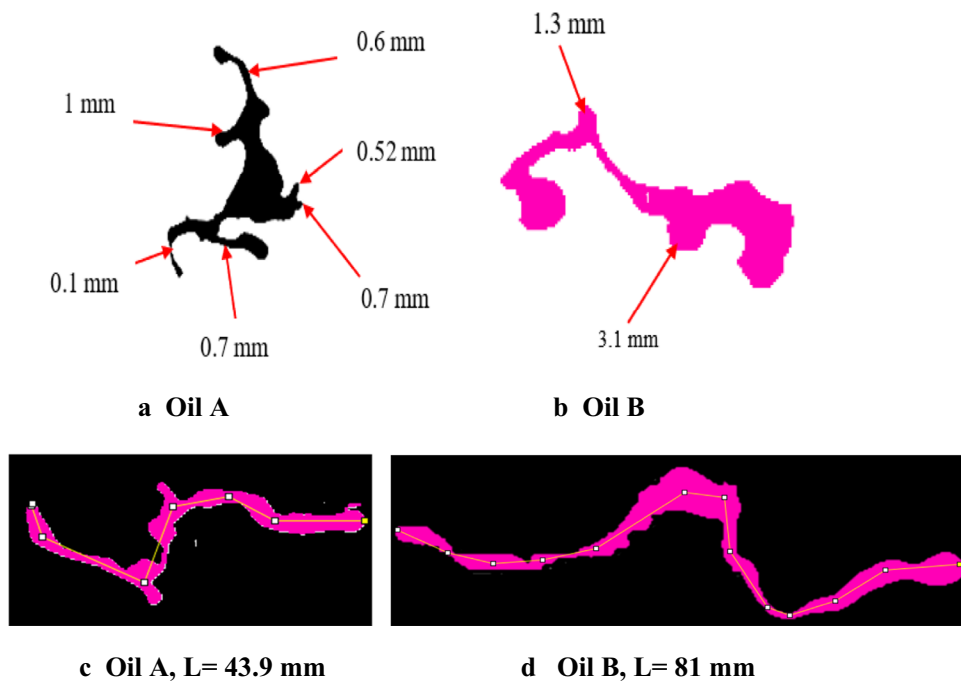


Fig. 8 Av. No. of daughter drop vs. Re (error bars = av. deviation)

The effect of Re on the deformation scale for each oil type that has been indicated by the aforementioned figures, needs to be interpreted based on the physical properties and turbulence stresses in the turbulent field of a stirred tank. The increase in the deformation scale with increasing Re of both oils is ascribed to the increased intensity of turbulent structures that have high kinetic energy (Nambiar et al. 1990; Calabrese et al. 1986; Sanjuan-Galindo et al. 2015; Hasan 2017). When these turbulent eddies collide with the slowly moving drop, it causes increased deformation for different reasons. First is the effect of turbulent pressure fluctuations on the drop surface, which is termed particle-eddy collision (Hinze 1955; Zhou and Kresta 1998; Hasan 2022; Hamad et al. 2023). This collision causes a transfer of energy from the high energy eddy to the drop which leads to stretching the drop to an extent that depends on the time of contact and the level of energy transferred (Paul et al. 2004; Andersson and Andersson 2006; Tran et al. 2021). The smaller turbulent eddies are responsible for the drop deformation, while large ones cause the transport of the drop (Paul et al. 2004; Nachtigall et al. 2016). If, the time of contact between the eddy and the drop is enough for sufficient energy transfer from the eddy to the drop, the drop experiences breakage (Hasan and Krakau 2017). In this current work, all breakages are seen to occur after forming a very thin neck. If the level of energy is low or the time of contact is less than the eddy lifetime, the drop experiences deformation only without breakage (Hasan and Krakau 2017). The second reason for drop deformation is the velocity gradient across the interphase between the drop and the continuous phase interphase. This velocity gradient increases the drag force exerted by the continuous phase or by the blade on the drop. As a response to the drag force, the drop experiences stretching depending on the velocity difference between the drop and the continuous phase (or the blade). When the drop becomes very close to the blade, the velocity difference is highest, so, the deformation becomes highest, as has been presented in Fig. 3. High speed videos show that deformation is very low below and above the blade, even at high Re , but it is highest in front of the blade or in between the blades. This is because of the high strength of flow currents ejected from the blade tip normal to the tank wall, as has been reported by previous studies (Agarwal 2021; Maluta 2023). High deformation shearing effects at the blade's tip and between blades have been reported in previous work (Kumar et al. 1991; Sanjuan-Galindo et al. 2015; Alabdly et al. 2020).

The difference in the deformation scale behavior between A and B is attributed mainly to the difference in physical properties, mainly the viscosity, because the difference in surface tension is small. The lower viscosity drop (A) causes a high viscosity difference with the continuous phase (water). This leads to an increased interaction between them, causing a high scale deformation of drop A (Arai et al. 1977;

Fig. 9 Stretching of oil A and B at 122330 (length is measured by image processing segment line)



Håkansson et al. 2022; Wang et al. 2022). In addition, the low viscosity of A, reduces the resistance of the drop to the disruptive forces exerted by flow currents.

Because of the higher viscosity (B), it exhibits a larger deformation scale before breakage than A. Higher viscosity of drop B increases stabilization against disruptive turbulent stress (Stamatoudis and Taviarides 1985; Calabrese, et al 1986; Håkansson et al. 2022). Therefore, the drop responds by amending its shape to reduce the effect of acting stresses and to hold its entity as much as possible. This leads to a larger extension before breakage. When the degree of oscillation increases to a value that is able to make the surface unstable, the deformation reaches its maximum and the drop breaks up into a number of smaller drops (Lemenand et al. 2013; Hasan 2017). The role of viscosity is to reduce the interaction between the drop and the continuous phase, thereby reducing breakage probability. Therefore, this role of viscosity causes the number of daughter drops of oil B to be much lower than that of drop A.

Referring to Tables 3 and 4, it can be seen that some shapes are highly complicated with high deformation parameters (projection area ratio, projection perimeter ratio, and circularity), which produces a higher number of daughter drops often but not always. Table 3 for oil A at $Re = 6110$, shows that, in general, high deformation shape factors generate higher number of fragments. However, on some occasions, high deformation shapes give low number of daughter drops. In case 2, the perimeter increases by 3 times, producing 4 daughter drops, while in cases 3 and 9, the perimeter extends lower but the number of daughter drops is higher, which is 5. Table 4 for oil A at $Re = 12230$ shows that in case

5, the perimeter extends by 4 times, producing 40 fragments, while in case 13, it extends by 2.8 producing 49. In Case 14 in Table 6, the deformation reaches $PPR = 4.5$, producing only 3 fragments. The reason behind this is that the number of daughter drops is not solely dependent on the scale of critical deformation. After first breakage, there are several factors affecting the total number of produced daughter drops, such as the size of drops, the time the produced daughter drops spend in the impeller region (Hasan 2018a, b), and the local position of large daughter drops relative to the blade. If the daughter drops after the first breakage are large and close to the blade, they can easily break further, producing more daughter drops because of high turbulence level that affects the large drop more than the small drop (Hasan 2017). In addition, in some cases the daughter drops produced from the first breakage, stay for prolonged period of time retained by flow currents and vortices close to the blade, giving the opportunity to a produce high number of fragments (Andersson and Andersson 2006; Hasan 2018a, b). All these factors are dependent on the complicated motion of turbulent eddies in the stirred tank, which is intermittent and highly random.

Shape factors, such as circularity and aspect ratio (major/ minor diameter), have been used by several studies (e.g., Hinze 1955; Clift et al. 2005; Nachtigall et al. 2016) to describe the degree of deformation of fluid particle (drop or bubble) in flow systems. The use of different shape descriptors to describe the deformation behavior of drops in a specific system, provides a better understanding for this phenomenon. In order to understand the physical significance of each shape descriptor used in this work, it is necessary to analyze the individual behavior of each deformed

shape in Tables 4, 5 and 6. The average values (in Figs. 5, 6 and 7), give the overall trend but not the specific trend, of each shape descriptor. On some occasions, different trends between the three shape factors are noticed. Tables 4, 5 and 6 indicate that there is a difference in the behavior between these three shape descriptors, indicating the difference in physical significance of each shape descriptor. For example, observing Figs. 5, 6 and 7 indicates that at $Re = 12230$, for oil A, the average circularity decreases to 0.23 (77% change), the average surface area increases by 88%, and the average perimeter increases by 305%. This means that each one addresses a particular physical phenomenon; as not all of them change by the same percentage. Additionally, comparing case 1 with case 2 in Table 2 shows that PAR and PPR are lower for case 2, indicating the lower deformation. However, these cases show that the circularity of case 2 is also lower, indicating a higher deformation. The same behavior can also be noticed for several cases in the three tables. There are also a few occasions in which the trend of the perimeter extension differs from that of the surface area extension as can be seen when comparing cases 6 and 7 in Table 6. This indicates that for case 6, the PAR is higher than that of case 7 but the PPR is lower. Therefore, it is of scientific significance to express the fluid particle deformation for a certain system by using different shape descriptors. This is because each shape descriptor can address a certain deformation aspect. The circularity expresses the deviation from the original circular shape (or from sphericity in a three-dimensional system). The perimeter extension mainly addresses the elongation deformation by quantifying the increase in filament length. The surface area extension addresses the increase in drop surface area, which plays an important role in heat and mass transfer. Strictly speaking, the most suitable shape descriptor to express the deformation scale depends on the specific characteristics of the dispersed phase and on the application. It is more appropriate to use different shape descriptors for characterizing and quantifying the deformation aspects of fluid particles in turbulent dispersion. This is because of the complicated hydrodynamics governing fluid particle motion in turbulent fields.

The images of the deformed shapes presented in Tables 4, 5 and 6, reveal that:

- 1) More thin branches are observed in the deformed morphology of drop A than in drop B. Figure 9 compares selected examples of the number and thickness of these branches between drops A and B as characterized by image processing. Figure 9a shows the deformed shape of drop A with 6 branches of thickness ranging from

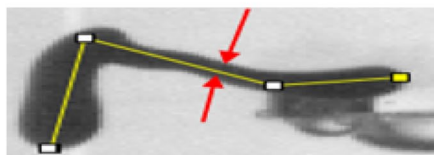
0.1 mm to 1 mm. While, Fig. 9b shows most branched shape seen for drop B with a lower number of branches with a larger thickness; these are the thinner branches seen for drop B. The more and thinner branches, produce a higher number of daughter drops because the branches are easy to cut by turbulent eddies.

- 2) Drop B experiences higher elongation deformation than drop A. Figures 9c and d compare the maximum elongation captured by the high-speed camera for both drops A and B. It can be seen that the elongation of drop B is higher than that of drop A by about 1.8 times. The high elongation of drop B is ascribed to its stabilization against the external turbulent stresses provided by viscous forces and coherence forces.

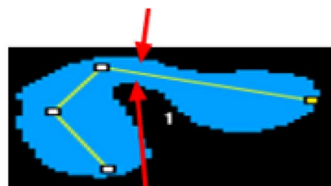
Highest deformation scale without breakage

High-speed images show that not all deformations lead to breakage. It is important to report the maximum degree of deformation seen at which the drop is still able to keep its entity without breakage, and how much the increase in surface area is at this degree of deformation. This is to understand the role of not-broken deformed drops in increasing the surface area, which has a direct influence on transport phenomena. The maximum deformation without breakage is characterized by determining the length of the extended drop and the minimum thickness of the drop filament that can be reached without the occurrence of breakage. This thickness represents the minimum filament thickness at which the drop is still able to regain its original shape without breakage. In other words, any further decrease in this thickness makes breakage inevitable. Figure 10 shows the largest stretching and thinning seen at which the drop does not break up and restores its original shape. It is evident that the thinning of drop A (of $d_m = 6.3$ mm) reaches 1.2 mm and that of drop B (of $d_m = 6.5$ mm) reach 1.8 mm. Besides, the maximum length of drop A is 25.8 mm and for B is 16.5 mm. In other words, for drop A, when the thickness of the filament neck becomes less than 20% of its original diameter, the drop cannot keep its entity, and the breakage becomes certain. The relevant value of drop B is 28%. These values approach the findings of Andersson and Andersson (2006), for air bubble, who stated that the breakage occurs when the neck thickness reduces to 1/3- 1/2 mother bubble diameter. Håkansson et al. (2022), through theoretical simulation, reported that when the neck diameter becomes less than that of the smallest bulb of the two-bulbs drop, the breakup becomes certain. The factor that plays the major role beyond the ability of drop to restore its shape is the thickness of finest part along the filament length, coupled to the turbulence intensity. When

Fig. 10 Minimum thickness seen without breakage occurring at $Re=6110$



(a) Oil A, $d_m=6.3$, $th=1.2$ mm, $L=25.8$ mm, $PR=2.7$, $AR=1.87$, $th/d_m=0.20$



(b) Oil B, $d_m=6.5$, $th=1.8$ mm, $L=16.5$ PR=1.84, $AR=1.43$, $th/d_m=0.28$

the filament is thin, even low energy turbulent eddy can cut it and cause breakage. Figure 10 reveals that deformation can cause a considerable increase in the area even without breakage.

Drop viscosity and drop surface tension play an important role in breakage process in turbulent flow. The relative significance of each can vary on the conditions of the dispersion system and the level of turbulence. The viscosity of dispersed drop affects its breakage behavior by influencing the internal flow dynamics inside the drop (Hinze 1955; Clift et al. 2005). Higher viscosity tends to resist the breakup by stretching and deformation trying to reduce the effect of turbulent forces. The surface tension is responsible of holding the drop entity by minimizing its surface area which plays important role in maintaining its spherical shape and also resist the disruptive forces. Higher energy level is required to break drops with high surface tension. Therefore, dispersed phase with high surface tension generate larger drop size when breaking up (Maxworthy 1976; O'Rourke and Amsden 1987).

For the current work, because the difference in surface tension between drop A and B is small, the difference in deformation and breakage behavior is mainly ascribed to the effect of viscosity, which plays a major role in the dynamic drop behavior and in the quantitative values obtained.

Breakage time

Clift et al. (2005) defined the breakage time as the time taken from the moment when the deformation becomes 10% until the first breakage. In this current work, this time is considered the time interval starting from the moment at which the circularity of the drop image projection is 0.9, until the first breakage. The circularity is directly calculated by image processing software (Image J). It has been shown in Fig. 3 that, when the drop approaches the impeller, its circularity decreases to 0.9 approximately at the mid-distance between the blade and the impeller and decreases appreciably when it becomes close to the blade tip. After the first breakage, and due to the high turbulence level, the produced drops may continue breaking, producing further daughter drops. The interval between the first and last breakages, that produced the final number of daughter drops, is the “breaking interval”. This interval was reported to be a function of Re and mother drop size (Hasan and Krakau 2017). It involves the production of different size daughter drops, which can undergo further deformation scales, leading to further breakages. Figure 11 shows a typical example of the time behavior of the crude oil drop (A) from the injection moment until the final breakage, for $Re=12230$. It shows that after injecting the mother drop by 190 ms, the circularity (θ) reaches 0.9,

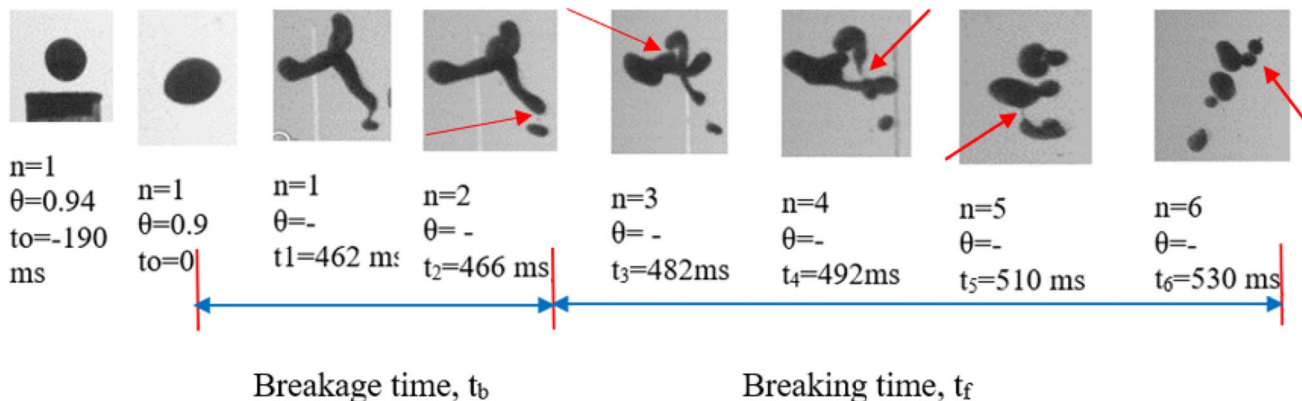


Fig. 11 Time behavior of breaking drop showing breakage and breaking times, oil A, $Re=12230$

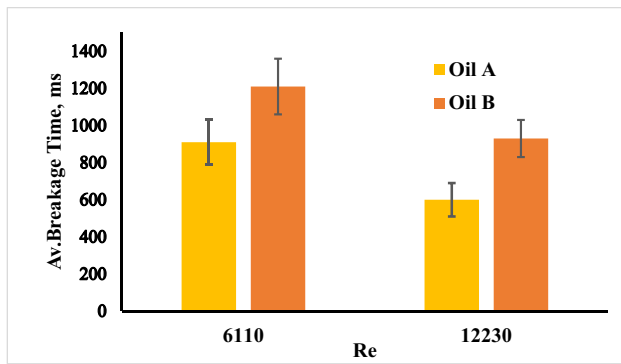


Fig. 12 Breakage time vs. Re for two oil drops (error bars = Av. deviation)

due to approaching the impeller region. This time instance (t_0) is the beginning of breakage time (Konno et al. 1983; Maass and Kraume 2012; Hasan and Krakau 2017). When the drop becomes very close to the blade, its shape becomes highly deformed prior to breakage; after 462 ms. Then the first breakage occurs after 466 ms from t_0 . After this first breakage, the drop breaks up further for a longer time, reaching the final breakage after 530 ms. Therefore, the total time taken from the 10% change in the circularity is 530 ms, the breakage time is 466 ms, and the breaking time interval is 64 ms during which, more 4 drops are generated. In this manner, breakage time and breaking interval are determined using time recording of a high-speed camera for the entire range of Re for both oil drops. The results are presented in Figs. 12. The result presented for each Re is the average of 100 breakages.

Figure 13 indicates that the average breakage time decreases clearly with Re, and is lower for oil A (crude oil). When Re is approximately doubled, the decrease in the breakage time is 34% for oil A and 23% for oil B. Increasing Re, causes an increase in the kinetic energy of the turbulent eddies and an increase in the velocity difference between the

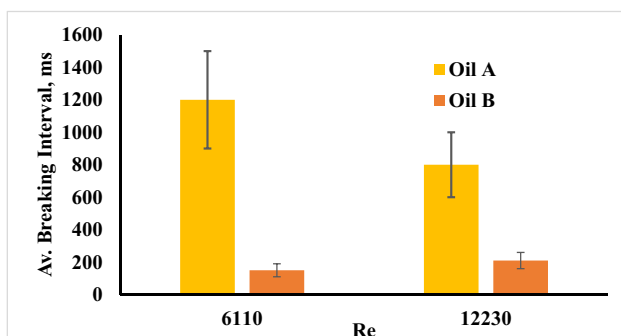


Fig. 13 Average breaking interval vs. Re for two oils (error bars = Av. deviation)

drop and the continuous phase (Lemenand et al. 2013; Liao and Lucas 2009; Hasan and Krakau 2017). In addition, it increases the probability of a collision between the drop and the fluid vortices (Andersson and Andersson 2006). These factors accelerate the deformation, leading to breakage in a shorter time. Figure 13 reveals that the breakage time of oil B is higher than that of drop A. This reveals the role of the higher viscosity of drop B in delaying its breakage. The higher viscous forces that contribute to resisting the disruptive forces (Andersson and Andersson 2006; Hasan 2017; Mhawesh et al 2022) lead to a delay in the breakage and to an increase in deformation time. Due to the low viscosity of drop A, it deforms quickly, reaching the breakage stage in a shorter time than B.

Figure 13 presents the values of the average breaking time interval between first and last breakages, for different Re and oils. For the range of Re, this interval of drop A is larger than that of drop B. This is due to the fact that, the viscosity of drop A, cause its breakages to last for a longer time. However, the effect of Re on this interval is different for each oil. For oil A, the breaking interval decreases with increasing Re, while for oil B, it increases with increasing Re. This behavior can be interpreted through the visualization of drops behavior. After the first breakage, the produced daughter drops stay exposed to the impeller effect, which leads to deform and break them further depending on Re and their sizes. For oil A, at lower Re, the daughter drops keep breaking slowly, even if it becomes far from the impeller, due to its low resistance to turbulent forces. At high Re, the subsequent breakages occur quickly, spending shorter time. For example, for a certain drop at Re = 6110, the time from the production of the first daughter drop to the 4th one (which is the last one), is 518 ms. While, at Re = 12230, the drop shown in Fig. 11, takes 64 ms between the first breakage and the last breakage, producing 6 daughter drops. This is because at higher Re, the high energy level increases the breakage frequency quickly, while at lower Re, the breakage frequency is slow and the drops take longer to break further.

For oil B, by observing the drop subsequent breakages times and locations, it is deduced that, at lower Re, the locations of first and last breakages are very close to each other with a very short time between them. They are observed to occur at the blade's tip. Therefore, the time taken between first and last breakage is shorter. It is observed that, when the daughter drop moves slightly away from the impeller, the breakages stop often, and thus the time between the first and last breakage becomes short. This is why the breaking interval for oil B increases with Re. Breakages of oil drop A are seen at a distance 16 mm from the blade's tip, while the most distant breakage of drop B, is seen at 8 mm or less from the blade edge.

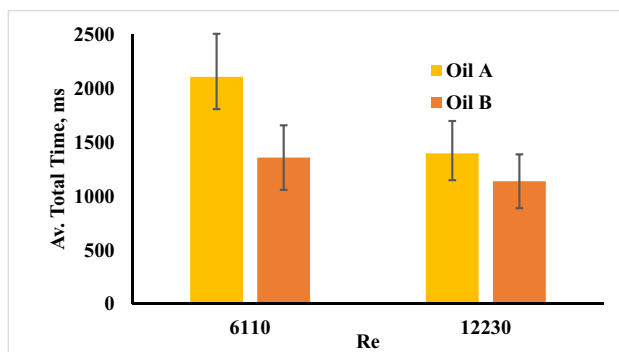


Fig. 14 Total time interval for 10% deformation until final breakage vs Re (error bars = Av. deviation)

Figure 14 shows the total time of the cascade breakage from initial deformation (0.9 circularity) to the last breakage. It can be seen that, there is a monotonic decrease with Re due the faster breakage caused by high turbulence level. In addition, the cascade breakage time for drop B is lower than that for oil A, because of the lower number of subsequent breakages.

Conclusions

The deformation scale and breakage time are direct functions of drop physical properties and Re in the turbulent field. The complicated deformed shapes of the drop captured by high-speed imaging can be successfully described by shape descriptors such as circularity, projection area, and projection perimeter using image processing software. Drop A of the lower viscosity, experiences a lower critical deformation scale than drop B of higher viscosity. Therefore, drop A easily deforms and quickly breaks up due to the lower stability against the turbulent stresses, resulting in a higher number of daughter drops. The shape descriptors indicate that drop B survives for a longer time and experiences a higher deformation scale prior to breakage, and when breaks up, it results in a lower number of daughter drops. High values of critical deformation of drop B are deduced, corresponding to a circularity of 0.07, a surface area increase of 2.9 times, and a perimeter extension of 5.5 times. These values are higher than drop A, which was observed to deform quickly, producing more fine branches morphology. 90% of the deformation scale occurs when the drop approaches the blade's tip or enters between blades. The breakage becomes inevitable when the neck thickness relative to the mother drop diameter is lower than 0.2 for oil A and 0.28 for oil B. The maximum deformation without breakage can increase the drop surface area appreciably (88% of B and 43% of A).

The breakage time is lower for drop A due to the low critical deformation. The breaking time interval (estimated from the first breakage to the last one) is longer for drop A because of the continuous breakages that persist for a longer time due to lower resistance to turbulent stresses. The breakage time decreases by 34% for drop A and 23% for drop B when Re is doubled. The longer survival of drop B is ascribed to the higher viscous forces that resist the disruptive forces and provide more stability against them. The use of different shape descriptors for characterizing deformation scale gives a better understanding of the phenomenon as each one can address a certain deformation behavior.

Nomenclature

A: Area, m²; *B*: Breakage rate, s⁻¹; *D_i*: Impeller diameter; *dm*: diameter of mother drop, m; *H*: Distance between the injection point and impeller, m; *n*: Number of drops; *N*: Rotational speed, rpm; *p*: Perimeter, m; *Re*: Reynolds Number; *t_b*: Breakage time, s

Greek letters

μ : Kinetic viscosity, kg/m.s; θ : Circularity; ρ : Density, kg/m³

Acknowledgements The authors acknowledge the Alexander von Humboldt Foundation/Germany for providing the necessary experimental tools for this work.

Declarations

Conflict of interest The authors declare that there is no conflict of interest regarding the publication of this article.

References

- Agarwal A (2021) Numerical investigation of flow behavior in double-Rushton turbine stirred tank bioreactor. *Materials Today: Proceedings* 43:51–57
- Alabdly HA, Majdi HS, Hamad MF, Hathal MM, Hasan BO (2020) Effect of impeller geometry on bubble breakage and the contributions of different breakage mechanisms in a stirred tank. *Fluid Dyn. Res* 52(6):65504
- Andersson R, Andersson B (2006) On the breakup of fluid particles in turbulent flows. *ICChE J* 52:2020–2030
- Andersson A, Helmi A (2014) Computational fluid dynamics simulation of fluid particle fragmentation in turbulent flows. *Appl Math Model* 38:17–18
- Arai K, Konno M, Mutunaga Y, Saito S (1977) Effect of dispersed-phase viscosity on the maximum stable drop size for breakup in turbulent flow. *J Chem Eng Jpn* 10:325–330
- Calabrese RV, Chang TPK, Dang PT (1986) Drop breakup in turbulent stirred-tank contactors, part I: effect of dispersed-phase viscosity. *AIChE J* 32(4):657–666
- Clift R, Grace JR, Weber ME (2005) *Bubbles, drops, and particles*, 2nd edn. Courier Corporation

- Coulaloglou CA, Tavlarides LL (1977) Description of interaction processes in agitated liquid–liquid dispersions. *Chem Eng Sci* 32(11):1289–1297
- Crowe CT (2005) *Multiphase flow handbook*, 1st edn. CRC Press, Boca Rotan
- Daub A, Böhm M, Delueg S, Büchs J (2013) Measurement of maximum stable drop size in aerated dilute liquid–liquid dispersions in stirred tanks. *Chem Eng Sci* 104:147–155
- Håkansson A, Brandt L (2022) Deformation and initial breakup morphology of viscous emulsion drops, in isotropic homogeneous turbulence with relevance for emulsification devices. *Chem Eng Sci* 253:117599
- Håkansson A, Crialesi-Esposito M, Nilsson L (2022) Brandt, criterion for when an emulsion drops undergoing turbulent deformation has reached a critically deformed state. *Colloids Surf* 648:129213
- Hamad MF, Hasan BO, Majdi HS, Craig RA, Alabdly HA, Hathal MM (2023) The local dependence of bubble breakup for different impeller geometries in a stirred Tank. *Iran J Sci Technol Trans Mech Eng* 47(2):469–479
- Hasan BO (2017) Breakage of drops and bubbles in a stirred tank: a review of experimental studies. *Chin J Chem Eng* 25(6):698–711
- Hasan B (2018) Experimental study on the bubble breakage in a stirred tank part 2: local dependence of breakage events. *Exp Therm Fluid Sci* 96:48–62
- Hasan B (2018a) Experimental study on the bubble breakage in a stirred tank part 2: local dependence of breakage events. *Exp Thermal Fluid Sci* 96:48–62
- Hasan BO (2022) Single bubble breakage in oil under stirring conditions. *Al-Nahrain J Eng Sci* 25(1):6–11
- Hasan B, Krakau F (2017) Experimental study on the bubble breakage in a stirred tank. Part 1. Mechanism and effect of operating parameters. *Int J Multiph Flow* 97:94–108
- Herzog MH, Francis G, Clarke A (2019) *Understanding statistics and Experimental Design*, 1st edn. Springer
- Hinze JO (1955) Fundamentals of the hydrodynamic mechanism of splitting in dispersion processes. *AIChE J* 1(3):289–295
- Karimi M, Andersson R (2020) Stochastic simulation of droplet breakup in turbulence. *Chem Eng J* 380:122502
- Konno M, Aoki A, Saito S (1983) Scale effect on breakup process in liquid–liquid agitated tanks. *J Chem Eng Jpn* 16(4):312–319
- Kumar S, Kumar R, Gandhi K (1991) Alternative mechanisms of drop breakage in stirred vessels. *Chem Eng Sci* 46(10):2483–2489
- Lemenand T, Dupont P, Valle D, Peerhossaini H (2013) Comparative efficiency of shear, elongation and turbulent droplet breakup mechanisms: review and application. *Chem Eng Res Des* 91:2587–2600
- Liao Y, Lucas D (2009) A literature review of theoretical models for drop and bubble breakup in turbulent dispersions. *Chem Eng Sci* 65(10):2851–2864
- Maass S, Kraume M (2012) Determination of breakage rates using single drop experiments. *Chem Eng Sci* 70:146–164
- Maluta F (2023) Hydrodynamics, power consumption and bubble size distribution in gas–liquid stirred tanks. *Chem Eng Res Des* 194:582–596
- Maxworthy T (1976) On the breakup of viscous drops in a turbulent airstream. *J Fluid Mech* 77(02):223–239
- Mhawesh AM, Hasan BO, Znad H (2022) Hydrodynamics of stirred Tank and bubble breakup Behavior Induced by Rushton Turbine. *Al-Nahrain J Eng Sci* 25(1):35–43
- Nachtigall S, Zedel D, Kraume M (2016) Analysis of drop deformation dynamics in turbulent flow. *Chin J Chem Eng* 24:264–277
- Nambiar D, Kumar R, Gandhi KS (1990) Breakage and coalescence of drops in turbulent stirred dispersions. *Sadhana* 15:73–103
- Ni R (2023) Deformation and breakup of bubbles and drops in turbulence. *Annu Rev Fluid Mech* 56:319–347
- O’Rourke PJ, Amsden AA (1987) The droplet deformation and breakup continuum-mechanical approach. *Int J Multiph Flow* 13(2):201–220
- Paul EL, Atiemo-Obeng V, Kresta SM (2004) *Handbook of Industrial Mixing, Science and Practice*, second edn. Wiley, New Jersey
- Perrard S, Rivière A, Mostert W, Deike L (2021) Bubble deformation by a turbulent flow. *J Fluid Mech* 920:A15
- Puncochar M, Ruzicka MC, Simcik M (2022) Bubble formation and deformation. *Chem Eng Sci* 260:117729
- Sanjuan-Galindo R, Soto E, Zenit R, Ascanio G (2015) Viscous filament fragmentation in a turbulent flow inside a stirred tank. *Chem Eng Commun* 202:1251–1260
- Solsvik J, Jakobsen HA (2015) Single air bubble breakup experiments in stirred water tank. *Int J Chem React Eng* 13:477–491
- Stamatoudis M, Taviarides LL (1985) Effect of continuous-phase viscosity on the drop sizes of liquid–liquid dispersions in agitated vessels. *Ind Eng Chem Process Des Dev* 24:1175–1181
- Tran BV, Ngo SI, Lim YI, Bae K, Lee DH (2021) Hydrodynamics of air–kerosene bubble column under elevated pressure in homogeneous flow regime. *Chin J Chem Eng* 33:190–202
- Wang C, Yi L, Jiang L, Sun C (2022) Turbulence drag modulation by dispersed droplets in Taylor–Couette flow: the effects of the dispersed phase viscosity. *J Fluid Mech* 952:A39
- Zedel D (2010) Experimental investigations on the influence of the system properties and the drop diameter on drop breakage. PhD thesis, Chemical Engineering Department, Technical University of Berlin, Berlin
- Zhang L, He L, Ghadiri M, Hassanpour A (2015) Effect of surfactants on the deformation and break-up of an aqueous drop in oils under high electric field strengths. *J Pet Sci Eng* 125:38–47
- Zhang L, Huang Z, Fu Y, Song R, Yi Z, Zhou Y, Han L (2024) Experimental study on the differences between bubble and drop breakages in agitated turbulent flows. *AIChE J* 70(7):e18442. <https://doi.org/10.1002/aic.18442>
- Zhou G, Kresta SM (1998) Correlation of mean drop size and minimum drop size with the turbulence energy dissipation and the flow in an agitated tank. *Chem Eng Sci* 53(11):2063–2079

Publisher’s Note Springer Nature remains neutral with regard to jurisdictional claims in published maps and institutional affiliations.

Springer Nature or its licensor (e.g. a society or other partner) holds exclusive rights to this article under a publishing agreement with the author(s) or other rightsholder(s); author self-archiving of the accepted manuscript version of this article is solely governed by the terms of such publishing agreement and applicable law.